IEEE Access
Multidisciplinary ⋮ Rapid Review ⋮ Open Access Journal

Received 4 March 2024, accepted 7 March 2024, date of publication 19 March 2024, date of current version 27 March 2024.

Digital Object Identifier 10.1109/ACCESS.2024.3377692

RESEARCH ARTICLE

A Magnetic Field Concentration Method for Magnetic Flux Leakage Detection of Rail-Top Surface Cracks

WENDONG GONG[1,5], MUHAMMAD FIRDAUS AKBAR[1], (Member, IEEE), GHASSAN NIHAD JAWAD[2], (Member, IEEE), NAWAF H. M. M. SHRIFAN[3,4], AND FENGQIN ZHANG[5]

[1]School of Electrical and Electronic Engineering, Universiti Sains Malaysia, Engineering Campus, Nibong Tebal, Pulau Pinang 14300, Malaysia
[2]Department of Electronics and Communication Engineering, University of Baghdad, Baghdad 10071, Iraq
[3]Faculty of Oil and Minerals, University of Aden, Shabwa, Yemen
[4]Lee Kong Chian Faculty of Engineering and Science, Universiti Tunku Abdul Rahman, Bandar Sungai Long, Kajang, Selangor 43000, Malaysia
[5]School of Urban Rail, Shandong Polytechnic, Jinan, Shandong 250104, China

Corresponding authors: Muhammad Firdaus Akbar (firdaus.akbar@usm.my) and Nawaf H. M. M. Shrifan (nawaf_83@hotmail.com)

This work was supported by the Ministry of Education Malaysia Fundamental Research Grant Scheme (FRGS) under Grant FRGS/1/2023/TK07/USM/02/1.

ABSTRACT Magnetic Field Leakage (MFL) is one of the prominent methods used to detect rail top surface cracks. However, it has been shown that detecting narrow rail top cracks is a major challenge because of their weak magnetic leakage fields. This paper proposes a method to enhance MFL signals by using magnetic field concentration sheets. First, a simulation model of a cylindrical magnet is designed to analyze the stability of magnetic concentration effects in a uniform magnetic field environment with sheets of different sizes and types. Next, the simulation process is extended to investigate the effects of the magnetic concentration sheets on the leakage fields resulting from rail cracks. Meanwhile, a magnetic circuit model is built to analyze the magnetic field concentration mechanism. To validate the proposed method, a data acquisition system and an inspection trolley equipped with a magnetic field concentrating sheet are designed to detect artificially produced cracks on a rail top surface. Experimental results show that the proposed method can enhance the magnetic leakage field strength resulting from the cracks and improve the signal-to-noise ratio of the MFL signals. These results prove the benefits of the proposed method to rail top inspection efforts by reducing the probability of missing minor cracks when using the magnetic field concentration method.

INDEX TERMS Rail top surface cracks, magnetic flux leakage detection, three-dimensional hall sensor, magnetic concentration method.

I. INTRODUCTION

Rails bear high mechanical loads from the wheel during the high-speed running process. Besides, rails are usually exposed directly to various natural environments. Therefore, there are many kinds of defects on the rail surface, including stripping, contact fatigue damage, crushing, corrosion, abrasion, cracks, and so on. The damage type is even more complex on other special parts of the rail, such as the weld and the turnout. The running speed and the load capacity increased because of the increased density of high-speed railways [1]. Consequently, the probability of rail damage, as well as the damage type, is prone to increase [2], [3]. Hence, big challenges are posed to traditional rail damage detection and monitoring technology [4], [5]. Along with the development of high-speed rail, rail flaw detection is important to ensure railway safety [6], [7].

Cracks on the rail top surface are difficult to detect because they are usually very narrow and irregular [8], [9]. From the view of fracture mechanics, rail defects are usually generated

The associate editor coordinating the review of this manuscript and approving it for publication was Wuliang Yin.

by rail fatigue cracking, expansion to internal injury, and eventually fracture, especially in welding parts [10]. Therefore, the detection of early cracks on the rail top surface is of great significance.

Different kinds of Nondestructive Testing (NDT) techniques have been applied to rail inspection and evaluation processes, each with its advantages and limitations. Such techniques include visual inspection, ultrasonic inspection, and electromagnetic inspection [11], [12], [13]. However, the cracks on the rail surface are usually narrow and long. Therefore, it is a big challenge to detect the cracks comprehensively and accurately. The ultrasonic NDT technique is good at detecting the damage inside the rail, but it is difficult to detect the rail surface. Moreover, it requires coupling agents, which limits the detection speed. Thus, it is difficult to meet the demand for rapid online detection of rail surface damage on high-speed rail lines [14], [15]. Though the machine vision NDT technique can quickly detect chunks and corrosion pits on the rail surface, there are still limitations when detecting tiny cracks on the surface [16], [17]. This is because the detection result is significantly affected by the environmental light and the dust on the rail surface. Magnetic flux leakage (MFL) inspection is a typical electromagnetic detection technique [18]. MFL testing is based on the fact that when a magnetic field is applied to a ferromagnetic material, the defect on the surface will cause a significant change in magnetic permeability in the test material. Therefore, the field leaks out of the material into the air beside the defects. Besides, the flux leakage can be measured by a magnetic field sensor and used to estimate the dimensions of the defect. This technique is non-polluting, and no coupling agent is required. Meanwhile, it is usually fast, highly reliable, and cost-effective [19]. The MFL detection method can also overcome the influence of the external environment, and it has high accuracy in high-speed detection. For these reasons, it has great advantages in the evaluation and nondestructive testing processes of rail top surface cracks.

Researchers have analyzed the magnetic flux leakage signal in time and frequency domains to investigate the distribution pattern of the signal for the cracks on the rail surface. The relationship between signal features and defect geometry was analyzed by methods such as regression analysis, neural networks, finite element simulation, and data fitting. In [20], the authors simulated the effect of motion-induced eddy currents on the MFL signals by a three-dimensional finite element method (FEM). Results have shown that the motion between the detection device and the rail generates two types of motion-induced eddy currents, which reduce the peak value of the leakage signal and spatially affect the leakage signal, especially the fundamental values along the rail in the transverse and vertical directions. In [21] and [22], the authors investigated the use of MFL technology for non-contact local fault detection and rapid inspection of rails. In [23], [24], and [25], the authors proposed a new magnetization method, simulated it with finite element software, and experimentally studied the MFL detection method for the depth of defects

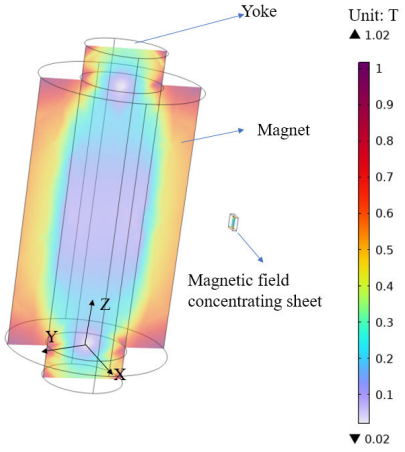

FIGURE 1. Finite element simulation model for testing the stability of the concentration effect.

near the surface of rails in high-speed railways. In [26], [27], [28], and [29], the authors carried out a lot of research in recent years in the areas of DC magnetic leakage detection, AC magnetic leakage detection, and pulse magnetic leakage detection for rapid rail movements. They have also analyzed the distribution pattern of slanting cracks and MFL signals and predicted the angle of the cracks by extracting the eigenvalues of the three-dimensional MFL signals. Besides, they analyzed the dynamic magnetization process of the rails under fast MFL detection, and the effects on the MFL signal were investigated when the material permeability and magnetoresistance changed. The magnetic leakage signal is weak because the cracks are usually narrow. Moreover, during the inspection process, the inspection device could be vibrated for kinds of unexpected reasons. This would significantly influence the magnetic leakage signal and result in imprecise outcomes. However, there is little information available in the literature about how to enhance the magnetic leakage field from the cracks on the rail surface.

This paper proposes a method to enhance the magnetic leakage field strength by using a magnetic field concentrating sheet. The stability of the magnetic leakage field concentrating effect is analyzed via finite element simulation and verified using experimental measurements. Meanwhile, an MFL detection simulation model and a magnetic circuit equation are established to analyze the magnetic field concentration mechanism. Finally, the effects of the magnetic field concentrating sheet are investigated in the MFL detection experiments for rail surface cracks.

The remainder of this paper is organized as follows: Section II establishes the finite element simulation model to analyze the stability of the magnetic field concentration effect in the uniform magnetic field environment using concentrating sheets of different sizes and materials, and builds the magnetic circuit model to analyze the magnetic field concentrating mechanism. Section III establishes the experimental platform to verify the simulation result by using the stability test platform and the MFL inspection of a rail sample

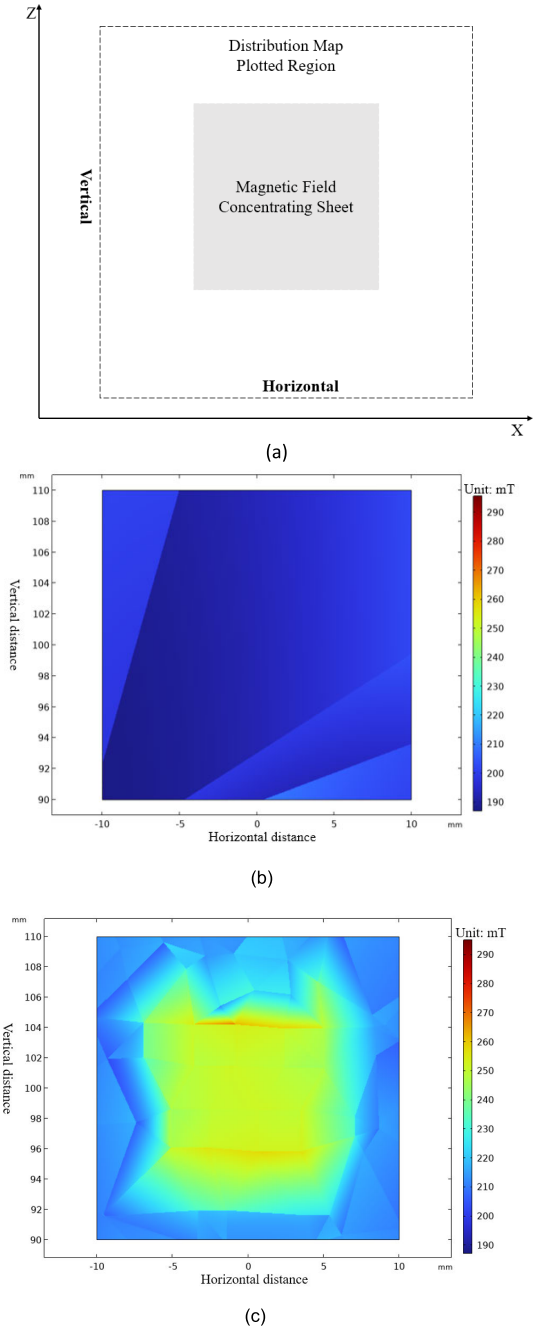

FIGURE 2. Magnetic field distribution map of concentration area (a)description of the mapping area(b)without concentrating sheet and (c)with concentrating sheet.

with artificial cracks on its surface. Section IV presents the conclusions of the simulation and experiment results.

II. SIMULATION OF MAGNETIC CONCENTRATING EFFECTS

A. STABILITY SIMULATION OF MAGNETIC CONCENTRATING EFFECTS

The finite element calculation is based on the vector partial differential equation of the electromagnetic field, combined with the material properties of the magnetization device

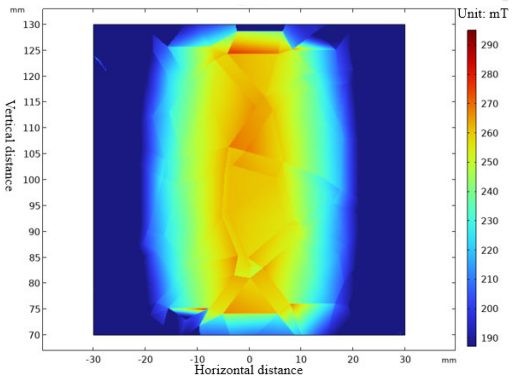

FIGURE 3. Magnetic field distribution map when the concentrating sheet was 50 mm in length and 50 mm in width.

and the object to be detected. The numerical solution of the leakage field is derived by meshing the cells and solving the nonlinear equation. Different types of finite element simulation software appeared with the development of computer technology. In this paper, COMSOL Multiphysics is chosen to perform the finite element simulation simulations. The simulation model was established to generate a uniform magnetic field environment, as shown in Figure 1.

In the model shown in Figure 1, a cylindrical hollow magnet model was created to generate a surrounding uniform magnetic field environment, and a yoke made of steel was placed in the middle of the magnet to enhance the magnetic field strength.

Magnetic field concentration means collecting the spatially distributed magnetic field and directing it into the detection area. The magnetic field concentration method was carried out by designing a thin sheet of ferromagnetic material of suitable size and material, as shown in Figure 1. The ferromagnetic sheet can increase the magnetic induction in its neighborhood since its magnetic permeability is much greater than the surrounding air. This process is equivalent to gathering the nearby magnetic fields together. Therefore, it can enhance the sensitivity of the detection.

The magnetic field concentration sheet was designed to be 10 mm long, 10 mm wide, and 3 mm thick. The initial length and width of the magnetic field concentration sheet is 5% of the cylinder length to reduce interference at the edge of the magnet. It was placed 100 mm from the outer surface of the magnet. Similarly, the initial thickness is 5% of the magnet diameter. The initial material was set to be Q235 carbon steel.

As shown in Figure 1, the origin of the coordinate system is the center of the cylindrical permanent magnet bottom, the X-axis direction is the direction of its length, the Y-axis direction is the direction of its thickness, and the Z-axis direction is the direction of the centerline of the cylinder. The magnetic field density distribution map was plotted in a region of 20 mm in length and 20 mm in width, located 1mm in front of the magnetic field concentrating sheet in

TABLE 1. Concentration effects in different size.

Concentration sheet size/mm		Enhanced religion(average size/mm, average magnetic density/mT)			
Length	Width	Length	Width	Density	Percentage increase
10	10	12.5	11.2	258.6	28.5%
20	20	23.6	16.1	259.2	28.8%
30	30	34.1	23.6	261.5	30.0%
40	40	44.9	29.7	263.8	31.1%
50	50	55.9	35.8	265.7	32.1%
60	60	66.7	39.1	269.9	34.1%

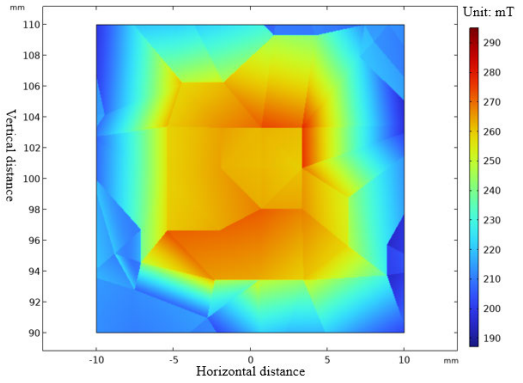

FIGURE 4. Magnetic field distribution map when the concentrating sheet was in 4mm thickness.

TABLE 2. Concentration effects in different thickness.

Concentration sheet size/mm	Enhanced religion(average size/mm, average magnetic density/mT)			
Thickness	Length	Width	Density	Percentage increase
1	11.5	10.9	223.2	10.9%
2	12.3	11.9	239.2	18.9%
3	14.1	12.6	258.6	28.5%
4	15.7	14.1	269.3	33.8%
5	16.9	15.4	277.4	37.9%
6	17.8	16.3	284.3	41.3%

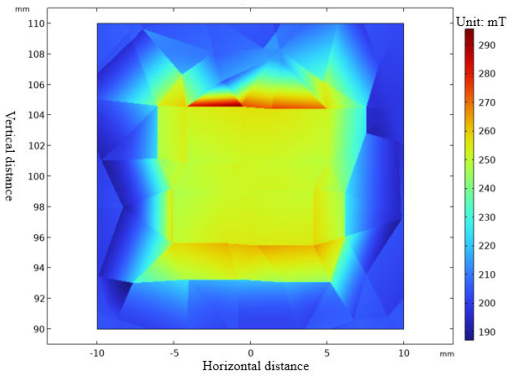

FIGURE 5. Magnetic field distribution map when the concentrating sheet was made of permalloy.

TABLE 3. Concentration effects in different material.

Concentration sheet size/mm	Enhanced religion(average size/mm, average magnetic density/mT)			
Material	Length	Width	Density	Percentage increase
Q235 steel	12.5	11.2	258.6	28.5%
Permalloy	12.8	11.9	262.8	30.6%
Industry pure iron	12.1	11.7	260.5	29.5%

each situation. The initial magnetic induction components of B_x, B_y, and B_z at the center of the region are 25.4 mT, 192.1 mT, and 54.1 mT, respectively. The results are shown in Figure 2.

As can be seen from Figure 2(a), the plotted magnetic field density distribution map was larger than the magnetic concentrating sheet. The vertical distance is along the Z-axis, and the horizontal distance is along the X-axis. It can be seen from Figure 2(b) and Figure 2(c) that the concentrating sheet can enhance the magnetic field. The average length of the magnetic field enhancement region was nearly 12.5 mm long and 11.2 mm wide. This shows that the concentration along the direction of the magnetic field is more effective. The average magnetic field strength in the region before enhancement is 201.2 mT, while after enhancement is 258.6 mT. The magnetic field enhancement region is not regular due to the nonlinear transition of the boundary at the edge. It was changed to 50 mm long and 50 mm wide while keeping the thickness at 3 mm to analyze the influence of the size of the concentration sheet. The magnetic field density distribution map was plotted in a region of 60 mm in length and 60 mm in width, located 1mm in front of the magnetic field concentrating sheet, as shown in Figure 3.

It can be seen from Figure 3 that the enhancement area is enlarged when the area of the concentrating sheet is increased. Meanwhile, length has a greater increase than width. The length of the enhanced area is about 55.9 mm, while the width is about 35.8 mm. It shows that the effect of field concentration grows faster along the direction of the magnetic field. Meanwhile, the enhancement effect was higher. The average magnetic field strength in the region after enhancement is 265.7 mT.

Furthermore, the concentrating effects when the magnetic field concentrating sheet is 3 mm thick and of different lengths and widths are shown in Table 1 below.

Table 1 shows that as the length and width of the concentration sheet increase, so do the length, width, and magnetic density of the enhanced region. However, the effect of the length is more significant than the width. It is because B_z is stronger than B_x.

To analyze the influence of the thickness of the concentration sheet, it was increased to 4 mm, while keeping the other dimensions to be 30 mm in length and 30 mm in width. The magnetic field density distribution map was plotted in a region of 20 mm in length and 20 mm in width, located 1 mm in front of the magnetic field concentrating sheet. The result is shown in Figure 4.

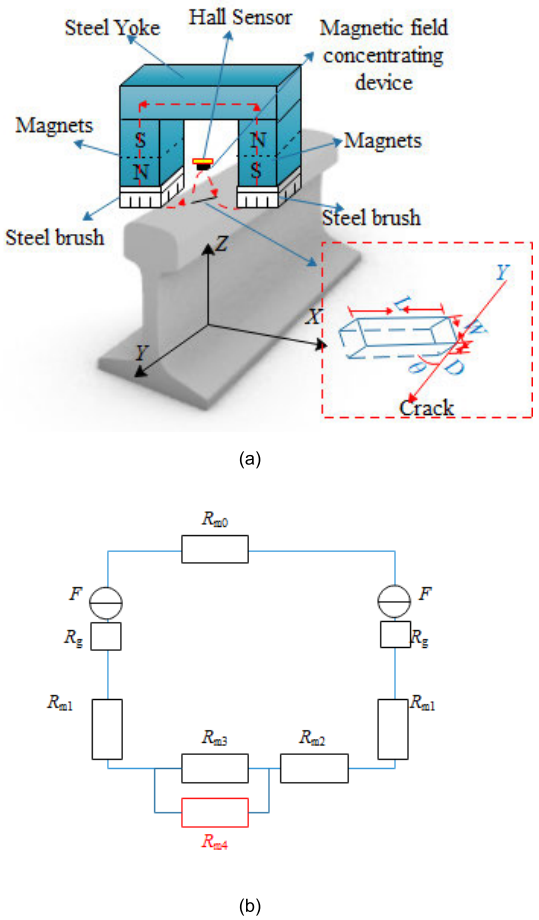

FIGURE 6. The structure and circuit of MFL detection device (a) structure, (b) circuit.

It can be seen from Figure 4 that the enhancement effects are strengthened when the thickness increases. The average length, width, and magnetic density of the enhanced-field region are 15.7 mm, 14.1 mm, and 269.3 mT, respectively.

The concentration effects when the magnetic field concentrating sheet is 10 mm long, 10 mm wide, and of different thicknesses are shown in Table 2 below.

From Table 2, it can be seen that as the thickness of the concentration sheet increases, so does the length, width, and magnetic density of the enhanced-field region. However, the effect is most significant. It is because B_z is stronger than B_x and B_y.

To analyze the influence of the material, the size of the concentrating sheet was set to 10 mm in length, 10 mm in width, and 3mm in thickness, while the material was changed to be a permalloy with model number 1J85, which has high initial permeability and small coercivity. Therefore, it can, in principle, respond quickly to changes in the magnetic field under a weak magnetic environment. The magnetic field density distribution map was plotted in a region of 20 mm in length and 20 mm in width, located 1 mm in front of the magnetic field concentrating sheet. The result is shown in Figure 5.

As can be seen from Figure 5, the concentration sheet made of permalloy has a more significant effect on enhancing the magnetic density. The average magnetic density of the enhanced religion is nearly 262.8 mT. However, the size of enhanced religion is nearly consistent with the previous results.

Industrial pure iron was also used to form the concentration sheet. The simulation results are shown in Table 3 below.

From Table 3, it can be seen that the better the magnetic conductivity, the more significant the effect of magnetic concentration.

B. MFL SIMULATION FOR RAIL CRACKS WITH MAGNETIC CONCENTRATION SHEET

Permanent magnets have been widely used in the MFL detection technique due to their simple structure, lightweight, and strong residual magnetic flux density [30]. Furthermore, it is difficult to continuously provide power for electrical magnets in the field inspection environment of steel rails. Therefore, two square NdFeB N52 permanent magnets were selected as the excitation source, and a U-shaped yoke made of Q235 steel was installed in the middle. The magnetic leakage field concentration sheet was chosen to be 1J85 permalloy material, and it was fixed on a pedestal made of plastic. The MFL detection structure and equivalent circuit model are shown in Figure 6.

As can be seen from Figure 6(a), steel brushes were fixed to the permanent magnet, and they were in close contact with the measured rail during the testing process to reduce the magnetic resistance from the air gap between the permanent magnet and the measured rail. The crack has four main parameters, including length, width, depth, and orientation. The length L is the distance along the direction in which the crack extends. The distance perpendicular to the length direction is defined as the width W. The depth D is defined as the distance down along the perpendicular to the rail surface. The orientation θ is defined as s the angle formed with the length direction and the Y-axis direction. The two permanent magnets with opposite excitation directions were finally connected with the yoke to form the excitation circuit. The hall sensor for acquiring MFL signals was fixed above the magnetic field concentrating device. Therefore, the magnetic field signal starts from the N pole of the left magnet, passing through the air gap area between the magnet and the rail. Then, it will go into the rail, and after encountering the crack defect, it will generate a magnetic leakage field signal. After that, the magnetic leakage field signal will pass through another air gap area between the crack and the concentrating sheet. Then, it will go into the concentrating sheet and in parallel with the air gap. After returning to the rail and passing through the other side, it encounters another air gap before reaching the S pole of the right magnet. The other side of the magnetic circuit is the magnetic field signal from the N pole of the right-hand magnet and returns to the S pole of the left-hand magnet after passing through the magnetic yoke.

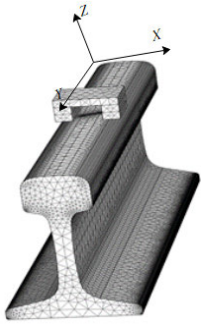

FIGURE 7. The meshing MFL simulation model.

According to the principle of magnetic circuit balance, the magnetic circuit should meet the following equation:

$$F = \phi \left(R_g + R_{m0} + R_{m1} + R_{m2} + R_{m3} \parallel R_{m4} \right) \quad (1)$$

Here, F is the total magnetic potential, R_{g} is the magnetic resistance of the magnets, R_{m0} is the magnetic resistance of the yoke, R_{m1} is the magnetic resistance of the air gap between steel brushes and the detected rail, R_{m2} is the magnetic resistance of the detected rail, R_{m3} is the magnetic resistance of the air gap between the crack and the sensor, and R_{m4} is the magnetic resistance of the concentration sheet. R_{m3} and R_{m4} are in parallel. It can be seen from (1) that the magnetic flux ϕ in the magnetic circuit is directly proportional to the magnetic potential F of the circuit and inversely proportional to the total magnetic resistance R_{m} of the circuit.

Both the yoke and the rail are made of ferromagnetic permeable materials. The air permeability is close to the vacuum permeability, which is much smaller than the permeability of ferromagnetic permeable materials. Therefore, R_{m3} is much larger than R_{m4}. The concentrating sheet can effectively reduce R_{m3} because it is in parallel with the air gap. Therefore, the total magnetoresistance will be reduced, and the magnetic flux ϕ can be effectively increased.

The three-dimensional (3D) model was established firstly in COMSOL multiphysics software for the finite element simulation, including the permanent magnets, the yoke, the steel brushes, the rail, and the cracks. This is followed by configuring the material properties of each component. Subsequently, the model meshed for calculation. The boundary of the crack was meshed in the triangular subdivision. Meanwhile, the cell size of the meshing model was fine to ensure the accuracy of the calculation. The meshing simulation model is shown in Figure 7.

Employing a sufficiently fine mesh can yield more accurate results, but excessively fine mesh division may lead to excessive computation time. The air region and the concentration sheet above the crack were set to be an extremely refined adaptive mesh method. Other parts of the model, including the yoke, magnet, steel brush, concentration sheet, and rail, were also meshed to be the free tetrahedral form, but set to be ultrafine refined adaptive mesh method. Since the magnetic leakage field is mainly concentrated at the junction of the crack and air, the boundary surfaces between the crack and the air were meshed in the form of free triangles. When the mesh grid cell size is smaller, the MFL simulation result will be more significant. However, when the grid is too small, it will lead to the very low speed of the finite element simulation. According to the comparative calculations, the limit mesh size of the crack and the air boundary surface was set to be 0.5 mm, and the boundary surfaces were divided into a total of 18918 boundary cells and 734 edge cells. The origin of the cartesian coordinate system was defined as the center of the crack on the rail surface, the X-axis direction was defined

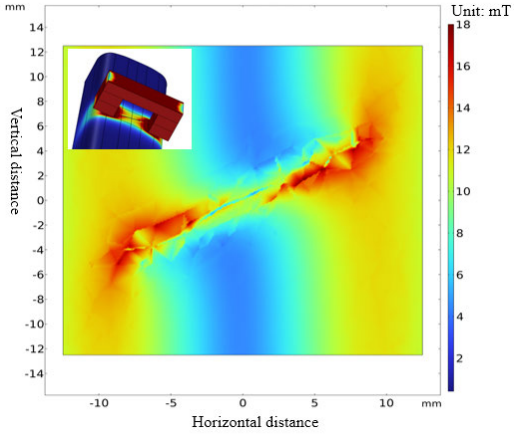

(a)

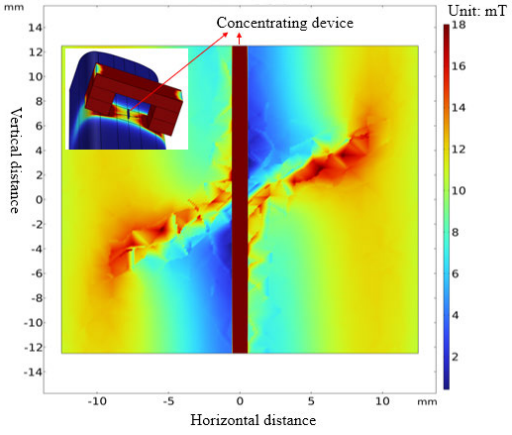

(b)

FIGURE 8. Magnetic field distribution map of crack (a)without concentrating sheet, and (b)with concentrating sheet.

TABLE 4. Concentration effects in different locations.

Location/mm		Without concentration /mT	With concentration /mT	Percentage increase
Horizontal	Vertical			
8.66	2.50	15.21	16.22	6.6%
4.33	1.25	14.78	15.64	5.8%
0	0	8.74	13.55	55.0%
-4.33	-1.25	14.92	15.27	2.3%
-8.66	-2.50	14.95	15.33	2.5%

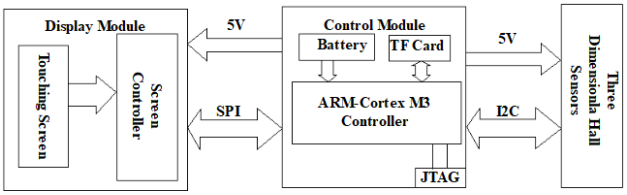

FIGURE 9. Structure of the magnetic field data acquisition system.

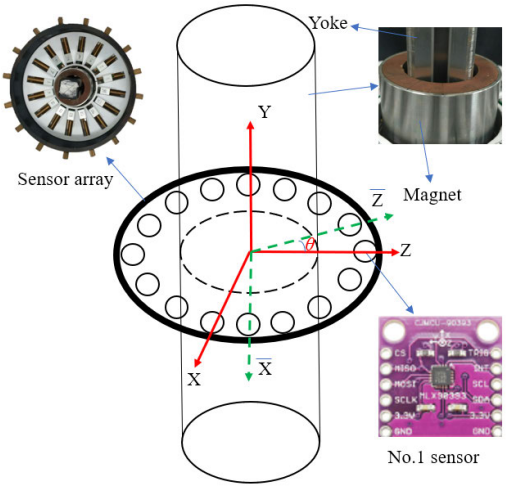

FIGURE 10. Stability test experimental platform.

as the direction perpendicular to the rail extension, the Y-axis direction was defined as the direction along the rail extension, and the Z-axis direction was defined as the direction perpendicular to the top surface of the rail. The spatial magnetic flux leakage field can be decomposed into B_x(along the X-axis direction), B_y(along the Y-axis direction), and B_z(along the Z-axis direction).

To analyze the effect of the magnetic field concentration sheet, the simulation results were compared with and without the concentration sheet, when the defect was 2 mm in width, 20 mm in length, 4 mm in depth, and 30° in angle. The magnetic concentration sheet was designed to be 10 mm in length, 10 mm in width, and 1 mm in depth. The distribution of total magnetic field B is shown in Figure 8.

It can be seen from Figure 8 that the concentration sheet can enhance the magnetic field, especially in the vicinity of the sheet. Five locations along the center of the crack were selected for comparison, and the data comparison results are shown in Table 4 below.

It can be seen from Table 4 that the simulation with concentration can enhance the magnetic leakage field. It can also be concluded that the concentration effect at the center is stronger than at the edges of the crack.

III. EXPERIMENTAL TEST

A. EXPERIMENTAL VERIFICATION OF STABILITY

A magnetic field data acquisition system was designed with a 16-bit precision MLX90393 three-dimensional hall sensor manufactured by Melexis with an output resolution

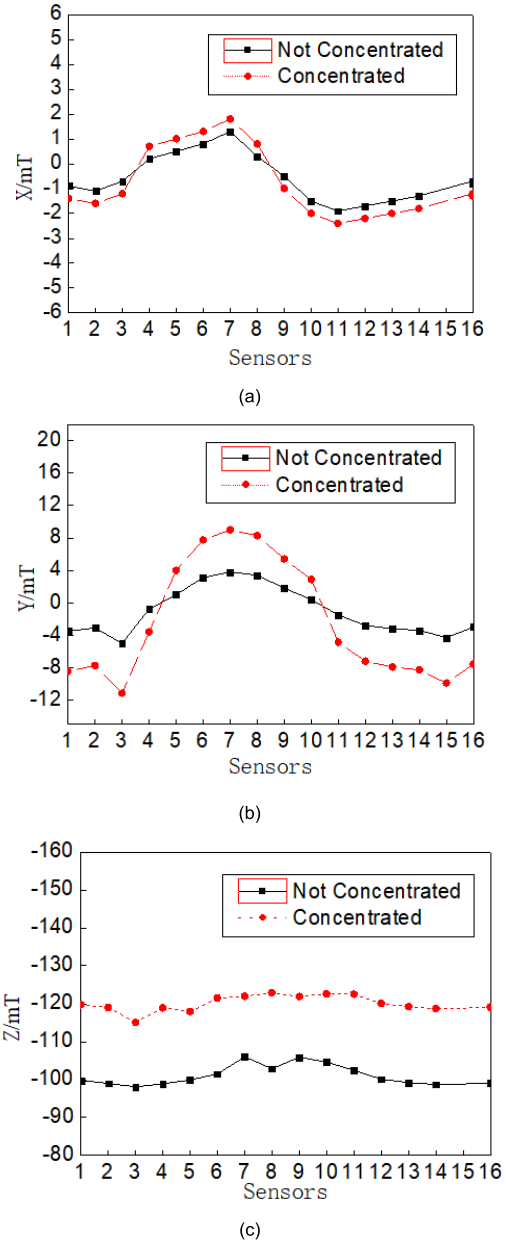

FIGURE 11. The magnetic field strength of the 16 sensors at a distance of 4 mm from the magnet,(a) B_x, (b) B_y, and (c) B_z.

of down to 0.16 μT/LSB(Least Significant Bit). The three-dimensional magnetic sensor communicated with an ARM microcontroller using the I2C protocol. The detected data were displayed in real-time on a touch screen and saved to a memory card. A block diagram of the magnetic field data acquisition system is shown in Figure 9.

A circular array of 16 three-dimensional magnetic sensors was evenly arranged around the hollow cylindrical magnet, and a nearly square yoke was placed in the middle of the hollow cylindrical magnet to enhance the magnetic field signal. The yoke is adjusted with the hole of the magnet, and it has the same effect as in the simulation model. To avoid interference, the bolts and other devices used to fix the sensors

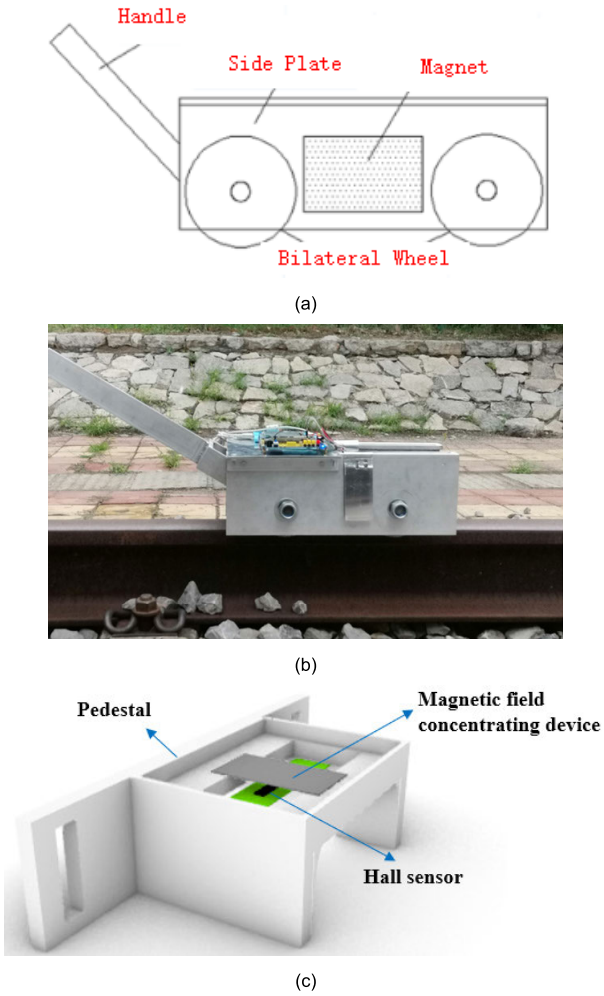

FIGURE 12. Inspection trolley, (a) Structure of inspection trolley, (b) Inspection trolley on the rail, and (c) Magnetic field concentrating sheet.

were made of copper, which is a non-ferromagnetic material. The concentrating sheet was fixed on the back of the PCB boards of the sensors. The experimental platform is shown in Figure 10.

In the experimental platform, the center point of the sensor array was defined as the origin of the coordinate system, the Y-axis direction as the direction along the axis of the cylindrical permanent magnet, and the X-axis and Z-axis directions were defined similarly to the magnetic field directions of sensor No. 1.

To conduct a comparative analysis of magnetic field data, it is necessary to unify the X, Y, and Z direction data detected by each sensor. Each sensor was evenly arranged around the magnet. The angle formed by either sensor with respect to sensor No. 1 is defined as θ. Since the Y-axis is always the same for all the sensors, the conversion equation for the X-axis and Z-axis is set below:

$$\begin{cases} \bar{z} = z * \cos\theta + x * \sin\theta \\ \bar{x} = x * \cos\theta - z * \sin\theta \end{cases} \tag{2}$$

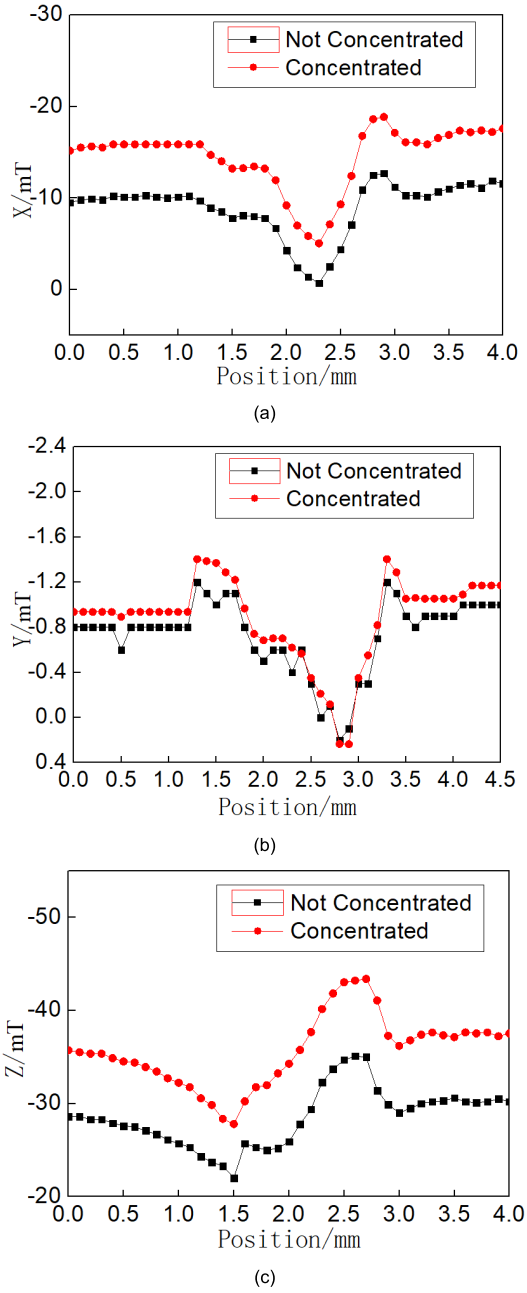

FIGURE 13. The MFL signals with and without the concentration sheet (a) B_x, (b) B_y, and (c) B_z.

Consequently, the X, Y, and Z directional magnetic field strengths of the 16 sensors at a distance of 4 mm from the magnet are shown in Figure 11.

It can be seen from the results that the magnetic field distribution was not completely uniform and symmetrical around the central magnets, with X-axis variations of [−1.9, 1.3], Y-axis variations of [−5.0, 3.8], and Z-axis variations of [−105.9, −98.1] without the magnetic field concentrating sheet. Meanwhile, with the magnetic field concentration sheet, the X-axis variation interval was [−2.7, 1.8], the Y-axis variation interval was [−11.2, 8.4], and the Z-axis variation interval was [−121.0, −114.3]. This proves that the effect of

TABLE 5. Concentration effects of defects in different size.

size/mm			Without concentration			With concentration		
L	W	D	A_{rx}	A_{ry}	A_{rz}	A_{rx}	A_{rx}	A_{rx}
10	1	3	1.65	0.21	4.98	1.92	0.26	6.05
10	2	3	1.69	0.22	5.02	1.93	0.26	6.11
20	1	3	2.47	0.31	6.43	2.89	0.32	7.52
20	2	3	2.49	0.32	6.48	2.90	0.33	7.53
10	1	4	1.89	0.25	5.22	2.01	0.28	6.35
10	2	4	1.95	0.26	5.23	2.09	0.30	6.39
20	1	4	2.73	0.35	6.72	3.17	0.39	7.96
20	2	4	2.84	0.40	6.81	3.25	0.47	8.04

the concentrating sheet on the magnetic field enhancement was significant and stable.

B. EXPERIMENTAL VERIFICATION OF MFL DETECTION

The inspection trolly was designed and fabricated to contain all the components used for the MFL inspection process. The trolly moves along a 75 mm-wide rail using double-sided wheels. An encoder was mounted on the trolly to record the relationship between the MFL data and the trolly's position on the rail, as shown in Figure 12.

A crack of 2 mm in width, 20 mm in length, 4 mm in depth, and 30° in angle was artificially machined by CNC(Computer Numerical Control) machine technology on the rail surface. The detected signals when inspecting this crack with and without the concentration sheet are shown in Figure 13.

It can be seen from Figure 13 that the background magnetic field and the amplitude of MFL signals were both shifted. To quantify the variation of MFL signal peak amplitude of the 3 components of the defect, the relative amplitude A_r was introduced, as follows:

$$A_r = \left|A_p - M\right| \tag{3}$$

In equation(1), A_{p} is the amplitude of the MFL signal, and M is the background magnetic field. It can be seen from the results that the magnetic leakage field is enhanced when using the concentration sheet, especially for B_{x} and B_{z}. The concentration effect for B_{y} is weak because the excitation direction is along the X-axis, and the magnetic leakage field is mainly along the X-axis and Z-axis. Therefore, B_{y} is negative and close to zero. The 30° crack angle is one of the most typical types. Thus, we focus on the 30° oblique crack in this paper. Moreover, the concentration effects of defects in different lengths (L), widths (W), and depths (D) were evaluated by the proposed method, as shown in Table 5 below.

It can be seen from Table 5 that MFL signal peak amplitudes of the 3 components of the defect increased. It shows that the concentration sheet can enhance both the background magnetic field and the peak amplitudes. Meanwhile, the relative amplitude A_r also be enhanced. Furthermore, the concentrating sheet did not change the trend of the magnetic leakage signal. However, the concentrating effect made the waveform of the magnetic leakage signal smoother.

IV. CONCLUSION

This paper demonstrates the effects of a magnetic field concentration sheet on the detected signals in the MFL inspection method. It is shown that the area and thickness of the sheet, in addition to its magnetic conductivity, can achieve better concentration effects and enhance the magnetic field in a uniform magnetic field environment. Furthermore, simulation and measurements show that the concentration sheet can enhance the magnetic leakage signal in each dimension while increasing its smoothness. This provides the possibility of further processing of the signals to reveal more information about the scanned surfaces.

REFERENCES

[1] Y. Zhao, Z. Liu, D. Yi, X. Yu, X. Sha, L. Li, H. Sun, Z. Zhan, and W. J. Li, "A review on rail defect detection systems based on wireless sensors," *Sensors*, vol. 22, no. 17, p. 6409, Aug. 2022.

[2] D. Bombarda, G. M. Vitetta, and G. Ferrante, "Rail diagnostics based on ultrasonic guided waves: An overview," *Appl. Sci.*, vol. 11, no. 3, p. 1071, Jan. 2021.

[3] C. Turner, A. Tiwari, A. Starr, and K. Blacktop, "A review of key planning and scheduling in the rail industry in Europe and UK," *Proc. Inst. Mech. Eng. F, J. Rail Rapid Transit*, vol. 230, no. 3, pp. 984–998, Mar. 2016.

[4] M. Ph Papaelias, C. Roberts, and C. L. Davis, "A review on non-destructive evaluation of rails: State-of-the-art and future development," *Proc. Inst. Mech. Eng., F, J. Rail Rapid Transit*, vol. 222, no. 4, pp. 367–384, Jul. 2008.

[5] U. Zerbst, R. Lundén, K.-O. Edel, and R. A. Smith, "Introduction to the damage tolerance behaviour of railway rails – a review," *Eng. Fract. Mech.*, vol. 76, no. 17, pp. 2563–2601, Nov. 2009.

[6] F. Fadaeifard, M. Toozandehjani, F. Mustapha, K. A. B. Matori, and M. Khairol, "Rail inspection technique employing advanced nondestructive testing and structural health monitoring (SHM) approaches—A review," in *Proc. Malaysian Int. NDT Conf. Exhib.*, Kualalampur, Malaysia, Jun. 2013, pp. 16–18.

[7] S. Santa-aho, A. Sorsa, A. Nurmikolu, and M. Vippola, "Review of railway track applications of Barkhausen noise and other magnetic testing methods," *Insight Non-Destructive Test. Condition Monitor.*, vol. 56, no. 12, pp. 657–663, Dec. 2014.

[8] M. Kostrzewski and R. Melnik, "Condition monitoring of rail transport systems: A bibliometric performance analysis and systematic literature review," *Sensors*, vol. 21, no. 14, p. 4710, Jul. 2021.

[9] A. Enshaeian and P. Rizzo, "Stability of continuous welded rails: A state-of-the-art review of structural modeling and nondestructive evaluation," *Proc. Inst. Mech. Eng., F, J. Rail Rapid Transit*, vol. 235, no. 10, pp. 1291–1311, Nov. 2021.

[10] S. Alahakoon, Y. Q. Sun, M. Spiryagin, and C. Cole, "Rail flaw detection technologies for safer, reliable transportation: A review," *J. Dyn. Syst., Meas., Control*, vol. 140, no. 2, Feb. 2018, Art. no. 020801.

[11] A. Poudel, B. Lindeman, and R. Wilson, "Current practices of rail inspection using ultrasonic methods: A review," *Mater. Eval.*, vol. 77, no. 7, pp. 870–883, 2019.

[12] Q. Li and S. Ren, "A visual detection system for rail surface defects," *IEEE Trans. Syst., Man, Cybern., C, Appl. Rev.*, vol. 42, no. 6, pp. 1531–1542, Nov. 2012.

[13] M. Masmoudi, S. Yaacoubi, M. Koabaz, M. Akrout, and A. Skaiky, "On the use of ultrasonic guided waves for the health monitoring of rails," *Proc. Inst. Mech. Eng., F, J. Rail Rapid Transit*, vol. 236, no. 5, pp. 469–489, 2022.

[14] H. Shi, L. Zhuang, X. Xu, Z. Yu, and L. Zhu, "An ultrasonic guided wave mode selection and excitation method in rail defect detection," *Appl. Sci.*, vol. 9, no. 6, p. 1170, Mar. 2019.

[15] S. Mariani and F. L. di Scalea, "Predictions of defect detection performance of air-coupled ultrasonic rail inspection system," *Struct. Health Monitor.*, vol. 17, no. 3, pp. 684–705, May 2018.

[16] X. Gibert, V. M. Patel, and R. Chellappa, "Robust fastener detection for autonomous visual railway track inspection," presented at the IEEE Winter Conf. Appl. Comput. Vis., Jan. 2015.
[17] J. Gan, Q. Li, J. Wang, and H. Yu, "A hierarchical extractor-based visual rail surface inspection system," *IEEE Sensors J.*, vol. 17, no. 23, pp. 7935–7944, Dec. 2017.
[18] F. Li, J. Feng, J. Liu, and S. Lu, "Defect profile reconstruction from MFL signals based on a specially-designed genetic taboo search algorithm," *Insight Non-Destructive Test. Condition Monitor.*, vol. 58, no. 7, pp. 380–387, Jul. 2016.
[19] P. Shi, S. Su, and Z. Chen, "Overview of researches on the nondestructive testing method of metal magnetic memory: Status and challenges," *J. Nondestruct. Eval.*, vol. 39, no. 2, pp. 1–37, Jun. 2020.
[20] G. Piao, J. Li, L. Udpa, S. Udpa, and Y. Deng, "The effect of motion-induced eddy currents on three-axis MFL signals for high-speed rail inspection," *IEEE Trans. Magn.*, vol. 57, no. 4, pp. 1–11, Apr. 2021.
[21] D. Kang, J.-T. Oh, J.-W. Kim, and S. Park, "Study on MFL technology for defect detection of railroad track under speed-up condition," *J. Korean Soc. Railway*, vol. 18, no. 5, pp. 401–409, Oct. 2015.
[22] G. Kim, M.-K. Seo, Y.-I. Kim, S. Kwon, and K.-B. Kim, "Development of phased array ultrasonic system for detecting rail cracks," *Sens. Actuators A, Phys.*, vol. 311, Aug. 2020, Art. no. 112086.
[23] A. G. Antipov and A. A. Markov, "Detectability of rail defects by magnetic flux leakage method," *Russian J. Nondestruct. Test.*, vol. 55, no. 4, pp. 277–285, Apr. 2019.
[24] A. G. Antipov and A. A. Markov, "3D simulation and experiment on high speed rail MFL inspection," *NDT E Int.*, vol. 98, pp. 177–185, Sep. 2018.
[25] A. G. Antipov and A. A. Markov, "Evaluation of transverse cracks detection depth in MFL rail NDT," *Russian J. Nondestruct. Test.*, vol. 50, no. 8, pp. 481–490, Aug. 2014.
[26] P. Wang, L. Xiong, Y. Sun, H. Wang, and G. Tian, "Features extraction of sensor array based PMFL technology for detection of rail cracks," *Measurement*, vol. 47, pp. 613–626, Jan. 2014.
[27] P. Wang, Y. Gao, G. Tian, and H. Wang, "Velocity effect analysis of dynamic magnetization in high speed magnetic flux leakage inspection," *NDT E Int.*, vol. 64, pp. 7–12, Jun. 2014.
[28] Y. Gao, G. Y. Tian, K. Li, J. Ji, P. Wang, and H. Wang, "Multiple cracks detection and visualization using magnetic flux leakage and eddy current pulsed thermography," *Sens. Actuators A, Phys.*, vol. 234, pp. 269–281, Oct. 2015.
[29] Y. Gao, G. Yun Tian, P. Wang, H. Wang, J. Ji, and S. Ding, "Ferrite-yoke based pulsed induction thermography for cracks quantitative evaluation," presented at the IEEE Far East NDT New Technol. Appl. Forum (FENDT), May 2015.
[30] W. Gong, M. F. Akbar, G. N. Jawad, M. F. P. Mohamed, and M. N. A. Wahab, "Nondestructive testing technologies for rail inspection: A review," *Coatings*, vol. 12, no. 11, p. 1790, Nov. 2022, doi: 10.3390/coatings12111790.

WENDONG GONG received the B.S. and M.S. degrees from Qingdao University of Science and Technology (QUST), in 2006 and 2012, respectively. He is currently pursuing the Ph.D. degree in rail nondestructive inspection with the School of Electrical and Electronic Engineering, Universiti Sains Malaysia (USM), Pulau Pinang, Malaysia. From 2006 to 2009, he was an Electrical Engineer with Omron Electronics LLC. From 2012 to 2023, he was a Lecturer with the School of Urban Rail, Shandong Polytechnic, China. His current research interest includes rail nondestructive inspection using magnetic flux leakage detection techniques.

MUHAMMAD FIRDAUS AKBAR (Member, IEEE) received the B.Sc. degree in communication engineering from International Islamic University Malaysia (IIUM), Malaysia, in 2010, and the M.Sc. and Ph.D. degrees from The University of Manchester, Manchester, U.K., in 2012 and 2018, respectively. From 2010 to 2011, he was with Motorola Solutions, Penang, Malaysia, as a Research and Development Engineer. From 2012 to 2014, he was an Electrical Engineer with Usains Infotech Sdn Bhd, Penang. He is currently a Senior Lecturer with Universiti Sains Malaysia (USM). He is also the Founder and the Director of the USM spin-off company, Visionlytics Sdn Bhd. His current research interests include electromagnetics, microwave imaging, non-destructive testing, and inspection systems.

GHASSAN NIHAD JAWAD (Member, IEEE) was born in Baghdad, Iraq, in 1984. He received the B.Sc. and M.Sc. degrees in electronics and communication engineering from the University of Baghdad, Baghdad, in 2005 and 2009, respectively, and the Ph.D. degree from The University of Manchester, in 2016. From 2006 to 2009, he was with Orascom Telecom Iraq (Zain Iraq later) as a Network Switching Engineer. He is currently a Lecturer with the University of Baghdad. His current research interests include microwave and millimeter-wave passive components, gyrotropic microwave devices, microwave nondestructive testing techniques, and short-range radar systems.

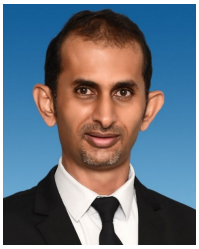

NAWAF H. M. M. SHRIFAN received the bachelor's degree in computer science and engineering from the University of Aden, Aden, Yemen, in 2006, and the M.Sc. and Ph.D. degrees from Universiti Sains Malaysia (USM), in 2017 and 2022, respectively. He is currently an Assistant Professor with the Lee Kong Chian Faculty of Engineering and Science, Universiti Tunku Abdul Rahman. His commitment to education is further demonstrated by his role as a Senior Lecturer with the Faculty of Oil and Minerals, University of Aden, Shabwah, Yemen. His current research interests include microwave nondestructive testing and computational intelligence algorithms.

FENGQIN ZHANG received the B.S. degree in railway vehicles from Dalian Railway College, in 1992, and the M.Sc. degree from Xian University of Architecture and Technology, in 2004. Since 1992, she has been with the School of Urban Rail, Shandong Polytechnic, China. She is currently an Associate Professor and takes charge of the School of Urban Rail as the Dean. She has published more than ten articles on rail transportation, published five textbooks, and obtained funding from many national projects.